Biomaterials Science

ROYAL SOCIETY OF CHEMISTRY

PAPER

View Article Online
View Journal | View Issue

Cite this: *Biomater. Sci.*, 2025, **13**, 4786

Image-guided embolization using Ta@Ca-Alg microspheres with optimized mechanical performance†

Peng Chen, [a] Shaphan Jernigan,[a] Keren Zhao,[a] George Varghese P J,[a] Mitesha Saha,[a] Charles Kim,[b] Amirhossein Arzani,[c,d] Gregory Buckner[a] and Jingjie Hu *[a]

Received 23rd May 2025,
Accepted 15th July 2025

DOI: 10.1039/d5bm00797f

rsc.li/biomaterials-science

Transcatheter arterial embolization (TAE) is a minimally invasive technique used to treat hypervascular tumors, hemorrhage, and vascular abnormalities. Though microspheres (MSs) have achieved widespread clinical use as embolic agents, they often lack imaging opacity, optimal morphology and mechanical properties which can lead to unpredictable trajectories, non-target delivery, and suboptimal embolization. This study developed tantalum-loaded calcium alginate (Ta@Ca-Alg) MSs with intrinsic radiopacity, tunable density, and mechanical properties. Ta@Ca-Alg MSs were synthesized using a gas-shearing method and analyzed for size, morphology, swelling behavior, density, radiopacity, and optimized mechanical properties. The results demonstrated that Ta@Ca-Alg MSs maintained a narrow size distribution, with increasing Ta concentration enhancing radiopacity to levels comparable with the clinical contrast agent OMNIPAQUE 350. Density and Young's modulus corresponding to different Ta concentrations were also investigated. Phantom model testing validated effective vessel occlusion and controlled penetration. *In vitro* hemocompatibility, sterility, and cytotoxicity studies confirmed excellent biocompatibility. These findings suggest that Ta@Ca-Alg MSs are a promising radiopaque embolic agent with optimized radiopacity, density, and mechanical properties, offering excellent potential for TAE procedures.

1. Introduction

Transcatheter arterial embolization (TAE) as a minimally invasive procedure has been widely utilized for tumor treatment clinically. Microspheres (MSs), as one of the most commonly used embolic agents, offer advantages such as controlled size distribution, targeted delivery, and the ability to achieve distal embolization.[1]

Calcium alginate (Ca-Alg) MSs have gained attention as promising embolic agents due to their biocompatibility, biodegradability, and their ability to be tailored for specific applications.[2] The core material of Ca-Alg MSs, sodium alginate, is a naturally derived polysaccharide. It forms a hydrogel matrix when crosslinked with divalent cations like calcium, creating a stable yet flexible structure suitable for embolization.[3–5] Calcium as the divalent cation is chosen to form crosslinked MSs with alginate due to its non-toxicity (naturally present in the human body) and its ability to be replaced by sodium ions in blood, making MSs biodegradable.[6] These MSs can be modified to achieve desired mechanical properties,[7] degradation rates,[8] and drug-loading capabilities,[9,10] making them attractive candidates for TAE applications.

During the TAE procedure, real-time imaging using fluoroscopy is required for monitoring the embolization process, as nontarget embolization can cause severe complications such as organ ischemia or stroke.[7,11,12] However, most commercially available embolic MSs lack inherent radiopacity. A common approach to address this issue is to mix the MSs with a radiopaque agent before injection.[13] This pre-mixing approach has several limitations, since only the contrast is visualized under fluoroscopy. If the particles settle or disperse unevenly, the contrast agent can travel further into the vascular network than the MSs, failing to accurately indicate their location. Additionally, the contrast agent is rapidly dispersed and absorbed from the target site, making it impossible to track the MSs postoperatively in the short or long term. Intrinsically

[a]*Department of Mechanical and Aerospace Engineering, NC State University, Raleigh, NC, USA. E-mail: jhu35@ncsu.edu*
[b]*Division of Vascular and Interventional Radiology, Department of Radiology, Duke University Medical Center, Durham, NC, USA*
[c]*Department of Mechanical Engineering, University of Utah, Salt Lake City, UT, USA*
[d]*Scientific Computing and Imaging Institute, University of Utah, Salt Lake City, UT, USA*

† Electronic supplementary information (ESI) available. See DOI: https://doi.org/10.1039/d5bm00797f

radiopaque MSs would overcome many of these limitations, allowing accurate visualization of the MS distribution during the procedure and in the long-term tracking using CT. Currently only a few commercially available MSs are inherently radiopaque. LUMI Beads (Boston Scientific, Marlborough, MA) are designed with inherent radiopacity by virtue of bonding to iodine. However, in clinical use, the level of radiopacity is fairly modest, requiring high radiation dose exposures or CT techniques for confident visualization. Emerging materials such as liquid metal embedded MSs have recently demonstrated intrinsic imaging capabilities across ultrasound, CT, and MRI without requiring additional contrast agents, offering alternative visualization methods.[14] While these materials offer promising alternatives for image-guided interventions, there remains a critical need for systematic comparisons of the radiopacity and imaging performance against clinically established contrast agents. Tantalum (Ta), a high-density transition metal, has been commonly used to create or enhance radiopacity in endovascular devices and liquid embolic agents due to its high radiopacity, inert chemistry, and long-term stability in biological environments.[15–17] By integrating Ta microparticles into Ca-Alg MSs, we aim to render the engineered MSs radiopaque for tracking under real-time fluoroscopic imaging, thereby improving procedural safety and efficacy.

The physical properties of MSs, such as size distribution and density, strongly influence embolic performance. While much research focuses on the size of MSs, this parameter alone cannot accurately determine the embolization behavior of the MSs.[18] While not yet well delineated, density also affects the administration and behavior of the MSs, given its degree of settling or buoyancy in the administration carrier and blood, flow behavior, and final deposition pattern in target vessels.[19] Moreover, if MSs settle too rapidly in the syringe, they may enter the delivery catheter unevenly, resulting in unpredictable administration.[20] The density also affects the Stokes number, which is an important parameter determining emboli trajectory and fate.[21] An optimal MS density ensures stable suspension, facilitating smooth delivery in microcatheter and travel through the blood vessels during embolization.[22] In this study, we also studied the tunability of density of the MSs based on the incorporation of Ta microparticles.

Another crucial aspect of embolic MSs is their elasticity (Young's modulus), which influences their ability to penetrate the microvasculature.[23] Optimizing these properties is vital for achieving a balance between sufficient deformability to smoothly navigate through microcatheters and vasculature, and adequate rigidity to resist deformation under physiological pressure, ensuring stable vessel occlusion. Excessively soft MSs risk fragmentation under hemodynamic stresses, potentially causing recanalization or unintended distal embolization. Conversely, overly rigid MSs might not effectively penetrate smaller vessels or may damage vascular structures, leading to procedural complications.[18,23] Limited studies have explored the incorporation of Ta into embolic MSs. For instance, Thanoo *et al.*,[16] introduced Ta into polyurethane MSs and evaluated their size distribution and hemocompatibility. Similarly, Zeng *et al.*,[15] embedded Ta into Ca-Alg MSs and examined their morphology and *in vivo* radiopacity using X-ray imaging. Despite these advancements, no prior study has systematically investigated the effect of Ta (contrast agent) loading on the mechanical properties of embolic MSs. This study addresses this gap by thoroughly characterizing how Ta concentration affects the MSs' mechanical properties, specifically targeting a modulus range closely matching human capillary elasticity. This is among the first systematic efforts to link Ta incorporation directly to tunable mechanical behavior in embolic MSs, potentially establishing novel standards for embolic MS performance. Fluidic force microscopy (FluidFM) has emerged as an advanced technique for measuring the nanoscale mechanical properties of soft materials, including hydrogels and MSs. FluidFM enables precisely force-controlled measurements in a liquid environment, closely mimicking physiological conditions.[24] Using FluidFM, we characterized the Young's modulus of Ta-loaded Ca-Alg MSs to assess how Ta incorporation affects their mechanical properties. This work helps ensure that the MSs maintain a balance between deformability for catheter passage and sufficient rigidity for stable embolization.

To evaluate the performance of embolic MSs under controlled, reproducible conditions prior to *in vivo* studies, phantom model testing is often used. Phantom models are designed to mimic human vascular anatomy and physiological conditions, allowing researchers to assess the distribution, and embolization efficiency of MSs in a simulated environment.[25] By using transparent, perfusable structures that replicate blood vessels, phantom models enable real-time visualization of MS flow, aggregation, and occlusion dynamics under specified flow conditions. Several phantom models and perfusion systems have been developed to investigate MSs for their embolic efficacy. Jernigan *et al.*[26] constructed an artificial surrogate of the liver tumor vasculature to experimentally investigate the effects of MS density and diameter on distal penetration. Miller *et al.*[27] developed an *in vitro* microvascular hepatic tumor model to compare the deposition characteristics of glass yttrium-90 MSs and traditional bolus administration methods. Miller *et al.*[28] developed a planar *in vitro* microvascular model of the hyper plastic hemiprostate to compare spatial distributions of radiopaque glass MSs, tris-acryl gelatin MSs, and polyvinyl alcohol nonspherical foam particles. Overall, phantom model testing serves as a critical preclinical tool that bridges the gap between *in vitro* characterization and *in vivo* animal studies, ensuring the safety and efficacy of embolic MSs before clinical applications. Despite the growing use of such models, no study to date has systematically compared embolic performance as a function of MS density and mechanical stiffness. The current study addresses this gap by introducing a robust *in vitro* platform for assessing how these physical parameters influence MS behavior during embolization.

In this study, we developed Ta@Ca-Alg MSs with tunable density, radiopacity, and mechanical properties to investigate their impact on embolization procedures. These MSs were syn-

thesized using a gas-shearing method[7] and characterized in terms of the size, morphology, swelling behavior, density, radiopacity, mechanical properties, and *in vitro* biocompatibility. Furthermore, we evaluated the embolization performance of the MSs in a physiologically relevant phantom model to assess their clinical applicability.

The findings of this study provide insights into the development of embolic MSs with enhanced imaging visibility, optimized mechanical properties, and controlled density, contributing to improved precision and efficacy in TAE procedures.

2. Experimental setup

2.1 Materials

Alginate acid sodium salt (medium viscosity), calcium chloride dihydrate, and phosphate buffered saline tablets were purchased from Sigma-Aldrich (St Louis, MO). Indocyanine green was obtained from Pfaltz & Bauer (Waterbury, CT). Sodium chloride was acquired from VWR Life Science (Solon, OH). Ta powder with an average size of 2 μm was sourced from Thermo Scientific, USA. Omnipaque™ (350 mg I mL^{-1}) was provided by GE Healthcare (Norway).

2.2 Methods

2.2.1 Synthesis of Ta@Ca-Alg MSs. The Ta@Ca-Alg MSs were synthesized (Fig. 1) using a previously established method in our group.[7] Sodium alginate (Alg) solution with a concentration of 1 wt% was prepared using a SpeedMixer (DAC 330–100 SE, FlackTek, Landrum, SC) at 3000 rpm for 10 minutes. Ta microparticles were then added to the Alg solution and mixed at 800 rpm for 5 minutes. The Ta@Alg solution was loaded into a 10 mL syringe and injected dropwise into 2 wt% calcium chloride solution at 0.05 mL min^{-1} using a syringe pump (LEGATO100, kdScientific, Holliston, MA). A 21/30 G concentric needle was used in between the syringe and the calcium chloride solution to generate micro droplets. Briefly, the Ta–Alg solution was injected through the inner layer of the needle, while air was directed through the outer layer of the needle at a flow rate between 783 ccm and 837 ccm. The MSs were formed immediately when the Ta@Alg droplets made contact with the calcium chloride solution placed 10 cm below the tip.

The MSs were named *x*Alg*y*Ca*z*Ta, where *x*, *y*, and *z* stand for the concentrations of sodium alginate, calcium chloride, and Ta in their original solutions respectively (Table 1).

2.2.2 Size and morphology of MSs. Images of MSs were obtained from an inverted microscope (Fisherbrand, Pittsburgh, PA). The diameters and roundness were analyzed using Fiji software.[29]

Roundness (eqn (1)) is a quantitative measure of how closely a given object's shape resembles a perfect circle, with a value closer to 1 indicating a more circular shape and a value closer to 0 signifying a more elongated or irregular shape.

$$\text{Roundness} = \frac{4 \times \text{area}}{\pi \times \text{major\_axis}^2}. \quad (1)$$

2.2.3 Swelling behavior of MSs. The MSs were immersed in saline for 48 hours. Images of the MSs were taken as described in 2.2.2 at 0, 1, 2, 4, 8, 12, 24, 48, 72 hours, and 6 months after immersion. The diameters of the MSs were analyzed using Fiji software. The swelling ratio was calculated using eqn (2)

$$\text{Swelling ratio} = \frac{\text{diameter of swelled MS}}{\text{diameter of unswelled MS}}. \quad (2)$$

2.2.4 Density of MSs. Stoke's law (eqn (3)) for settling velocity[30] was utilized for the measurement of MS density.

$$V_T = \frac{2r^2(\rho - \sigma)g}{9\eta} \quad (3)$$

Table 1 Naming and composition of MSs

MS	Sodium alginate (wt%)	Calcium chloride (wt%)	Tantalum (wt%)
1Alg2Ca0Ta	1	2	0
1Alg2Ca5Ta	1	2	5
1Alg2Ca10Ta	1	2	10
1Alg2Ca20Ta	1	2	20
1Alg2Ca30Ta	1	2	30

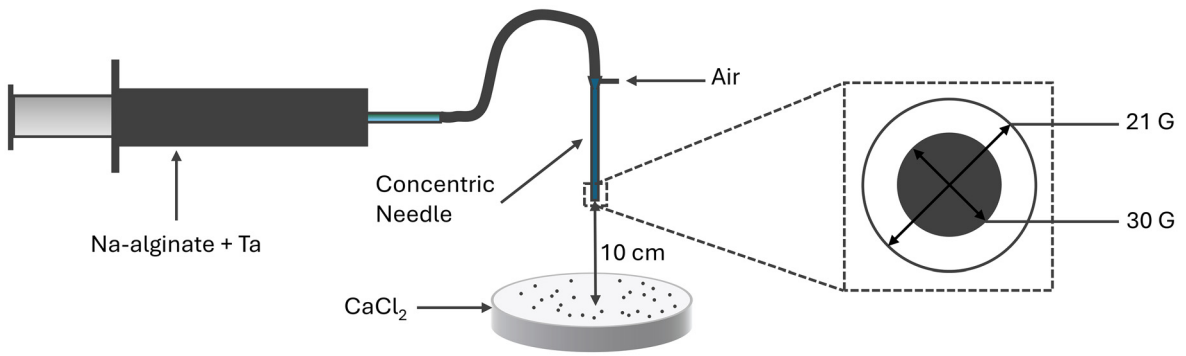

Fig. 1 Schematic apparatus of synthesis of Ta@Ca-Alg MSs.

where V_T is the settling velocity; r is the radius of the MS; ρ and σ are the densities of the MSs and the liquid, respectively; η is the viscosity of the liquid.

A measuring cylinder with 30 cm height was filled with deionized water. A single MS was gently placed onto the surface of the water. The settling time reflected how long it took the MS to descend from a height of 15 cm height to the bottom of the cylinder. A15 cm height was selected as the starting point to avoid the initial acceleration region. The settling velocity was calculated using the distance (15 cm) divided by the settling time.

1 mg mL^{-1} indocyanine green (ICG) as a fluorescent dye was loaded into the system (1Alg2Ca1ICG, developed in our previous work[7]) as the control of density measurement before and after swelling due to their ease of observation compared to the colorless MSs and the similar density (low ICG concentration) as the colorless MSs.

2.2.5 Radiopacity. The imageability of the MSs under X-ray was investigated using an AMI HTX system (Spectral Instruments Imaging, Tucson, Arizona, USA). 1× PBS solution, 1Alg2Ca0Ta, 50% OMNIPAQUE 350, and 100% OMNIPAQUE 350 were included as the controls. 1× PBS solution and 1Alg2Ca0Ta are two materials without contrast agents indicating no radiopacity, while 50% OMNIPAQUE 350 and 100% OMNIPAQUE 350 are two clinically used contrast agents, representing the lower end and upper end concentrations of OMNIPAQUE.[17] Image gray scales were analyzed using Fiji software.[29]

2.2.6 Mechanical properties of MSs using FluidFM. Fluidic force microscopy (FluidFM, Cytosurge, Glattbrugg, Switzerland) was used to measure the local Young's modulus (E) of MSs. The FluidFM system was composed of an atomic force microscopy (AFM) (Nanosurf FlexAFM, Liestal, Switzerland) and an MAT FluidFM micropipette (Cytosurge AG, Glattbrugg, Switzerland) with an 8 μm aperture and a 0.3 N m^{-1} spring constant. To perform nanoindentation tests on the Ca-alginate MSs, the micropipette (Fig. 2A) was combined with a 25 μm soda lime solid glass MS (Cospheric LLC, California) through the aperture with an 800 mBar pressure. The glass MS on the micropipette was then manually adjusted to the apex of the Ca-alginate MS (Fig. 2B). A 30 μm by 30 μm indentation area with 25 points on each Ca-alginate MS was tested. For each type of MS, 30 samples were tested. Each indentation was performed inside in a Petri dish containing the MSs in saline. To prevent MSs from moving laterally during testing, a nylon mesh with 200 μm openings was attached to the bottom of the Petri dish to physically hold the MSs.

The force–distance curves obtained from C3000 software (Nanosurf, Liestal, Switzerland) were then analyzed using Atomic J software.[31] Since the tip and the sample are both spherical, and the radius of the tip is much smaller than the sample radius, Hertz model (eqn (4)) was utilized to calculate Young's modulus:

$$P = \frac{4E}{3(1-\nu^2)}\sqrt{R}\delta^{\frac{3}{2}} \quad (4)$$

where P is the normal force applied between the tip and the MS; E represents Young's modulus; ν is Poisson's ratio; R is the radius of curvature at the apex of the tip; and δ denotes the indentation depth.

2.2.7 Sterility. To evaluate the sterility of MSs, 1 mL of each MS was added to 10 mL of LB broth in centrifuge tubes. LB broth alone served as a negative control, while LB broth inoculated with *Escherichia coli* (*E. coli*, ATCC 25922) was used as a positive control. The samples were then incubated overnight in an orbital shaker (C24 Incubator/Shaker, New Brunswick Scientific, Edison, NJ, USA) at 37 °C and 100 rpm. After incubation, the optical density of the suspensions was measured at 600 nm using a cell density meter (Ultrospec 10; Amersham Biosciences, Little Chalfont, UK). Each sample was tested in triplicate, with a total of six readings taken per test.

2.2.8 Cell viability. The biocompatibility of the MSs was assessed through an extraction assay following ISO-10993-5 guidelines,[32] using L929 fibroblasts (American Type Culture Collection (ATCC), Manassas, VA). The culture medium for L929 consisted of Dulbecco's Modified Eagle Medium (DMEM, Gibco BRL, Grand Island, NY, USA) supplemented with 10% heat-inactivated fetal bovine serum (Cytiva, Marlborough, MA) and 1% penicillin/streptomycin (Thermo Fisher Scientific, Inc., Waltham, MA). The L929 cells were incubated at 37 °C with 5% CO_2 and 95% humidity.

For the viability assay, the cells were seeded into 96-well plates at a density of 5000 cells per well and incubated for 24 hours. Extracts from selected MSs were prepared by incubating 1 mL of each type of MS in 10 mL of culture medium at 37 °C overnight. The supernatant was collected and diluted with culture medium to create extraction concentrations of 100%, 50%, 25%, and 12.5% (v/v). To assess potential cytotoxicity, L929 cells were exposed to these extract concentrations in their respective media. After 24 hours of incubation, cell viability was measured using the WST-1 assay (Cayman Chemical, Ann Arbor, MI, USA) according to the manufacturer's instructions. A 10% DMSO solution was used as positive control, while untreated cells served as the negative control. Three independent experiments were performed, with each experiment including four replicates for statistical analysis.

2.2.9 Live/dead assay. A live/dead cell assay was conducted with L929 fibroblast cells to evaluate cell viability in response to contact with the MS extracts. Positive and negative controls consisted of 10% DMSO and untreated cells, respectively. A live/dead assay kit (Invitrogen ReadyProbes™ Cell Viability Imaging Kit (Blue/Green), Thermo Fisher Scientific, Eugene, OR, USA) was used according to manufacturer's instruction. The cells were then imaged using a microscope (Leica DMi8, Germany). Three independent experiments were performed per test, with six randomly selected locations being imaged. The live (green) and dead (blue) cells were quantified using Fiji software (National Institutes of Health, Bethesda, Maryland).

2.2.10 Hemocompatibility. Hemolysis assay was performed to assess the interactions between MSs and blood. The hemolysis rate was determined according to the ISO 10993-4 stan-

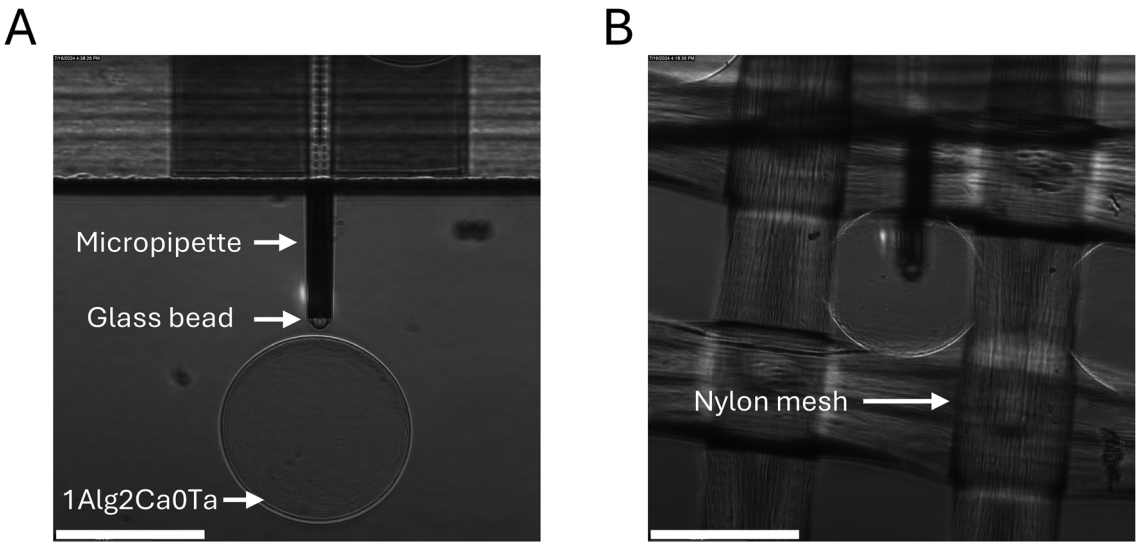

Fig. 2 Photographs of nanoindentation tests on a 1Alg2Ca0Ta MS conducted using FluidFM. (A) A micropipette combined with a 25 μm glass bead next to a 1Alg2Ca0Ta MS immersed in saline; (B) nanoindentation was performed on a 1Alg2Ca0Ta MS held on a nylon mesh with 200 μm openings. Scale bar: 200 μm.

dard.[33] Fresh citrated porcine blood (Lot # 24H52709, catalog # 7204906, LAMPIRE Biological Laboratories, Pipersville, PA) was diluted with 1× saline at a 4 : 5 ratio. For each MS type (1Alg2Ca0Ta, 1Alg2Ca5Ta, 1Alg2Ca10Ta, 1Alg2Ca20Ta), 0.5 g was added to 10 mL saline in a centrifuge tube (MS concentration: 50 mg mL^{-1}) and incubated at 37 °C for 30 minutes. Subsequently, 0.2 mL of the diluted blood was added to the tubes and incubated again at 37 °C for 60 minutes, followed by centrifugation at 3000 rpm for 5 minutes.

The supernatant was then transferred to a 96-well plate, and absorbance (A) at 545 nm was measured using a microplate reader (GENios, TECAN, Crailsheim, Germany). Positive and negative controls were prepared by mixing 0.2 mL of the blood with 10 mL of deionized water and 10 mL of PBS, respectively. The hemolysis rate was calculated using eqn (5).

$$\text{Hemolysis}\,(\%) = \frac{A_{\text{sample}} - A_{\text{negative control}}}{A_{\text{postive control}} - A_{\text{negative control}}} \times 100. \quad (5)$$

2.2.11 Phantom testing

2.2.11.1 Model design. A planar tumor model was designed to capture the multiscale physics of systemic circulation while matching physiological pressures and flow rates in large arteries down to the pre-capillary level. The resulting design consisted of 10 generations of channels which branched 2 times per generation. The dimensions of these channels were scaled with the inverse of the branching factor to prevent self-intersection. The inlet cross-section of the tumor model was 5.0 × 2.5 mm, which tapered down to only 18 μm at the outlet arterioles of the 10th generation. Vascular branches were mirrored about an axis passing through the inlet, resulting in a total of 2048 outlet arterioles, or 1024 outlet arterioles per side. The design of the microvascular model, which focused on achieving target tumor resistance, was aided both through analytical hydraulic resistance calculation and Computational Fluid Dynamics simulation (SolidWorks Flow Simulation, Dassault Systèmes, Vélizy-Villacoublay, France). Each polydimethylsiloxane (PDMS) model geometry was cast from a mold (40 × 40 mm footprint) fabricated using Two-Photon Polymerization (2PP) micro 3D printing technology (UpNano Gmbh, Vienna, Austria). The resulting hydraulic resistance was 146 PRU. Using methods similar to that of Miller *et al.* 2023,[27] it can be deduced that the resulting flow represents that of a 4.2 cm hepatic tumor with liver volume of 1400 mL, total liver flow rate of 160 mL min^{-1}, and tumor-to-normal uptake ratio of 8 : 1.

2.2.11.2 MS administration. To simulate a clinical embolization procedure, the tumor model was connected to an experimental setup (Fig. 3E), which was perfused with pulsatile flow of a water–glycerin mixture at a rate of approximately 1.8 cc s^{-1} and a pressure of 140/60 mmHg. The ratio of water to glycerin was tuned to approximate the dynamic viscosity of whole blood at 3.5 cP.[26,34] The vascular system consisted of a single branch of 3.2 mm (0.125 inch) inner diameter (ID) mated to a 1.6 mm ID tube leading to the tumor, and a bypass branch of 3.2 mm ID leading directly to the collection reservoir. The bypass branch is analogous to non-tumoral flow. The bypass flow rate was approximately 71 mL min^{-1} at a pressure of 140/60 mmHg. The tumor flow rate was approximately 35 mL min^{-1} at the outlet. Each single 0.5 mL aliquot of MSs was administered at a rate of 0.1 mL s^{-1} through a 2.4 F (0.022 in ID) 110 cm Terumo Progreat microcatheter (Terumo Corporation, Tokyo, Japan). The microcatheter was placed into the 1.6 mm caliber surgical tube just proximal to the tumor model. A computer-controlled syringe

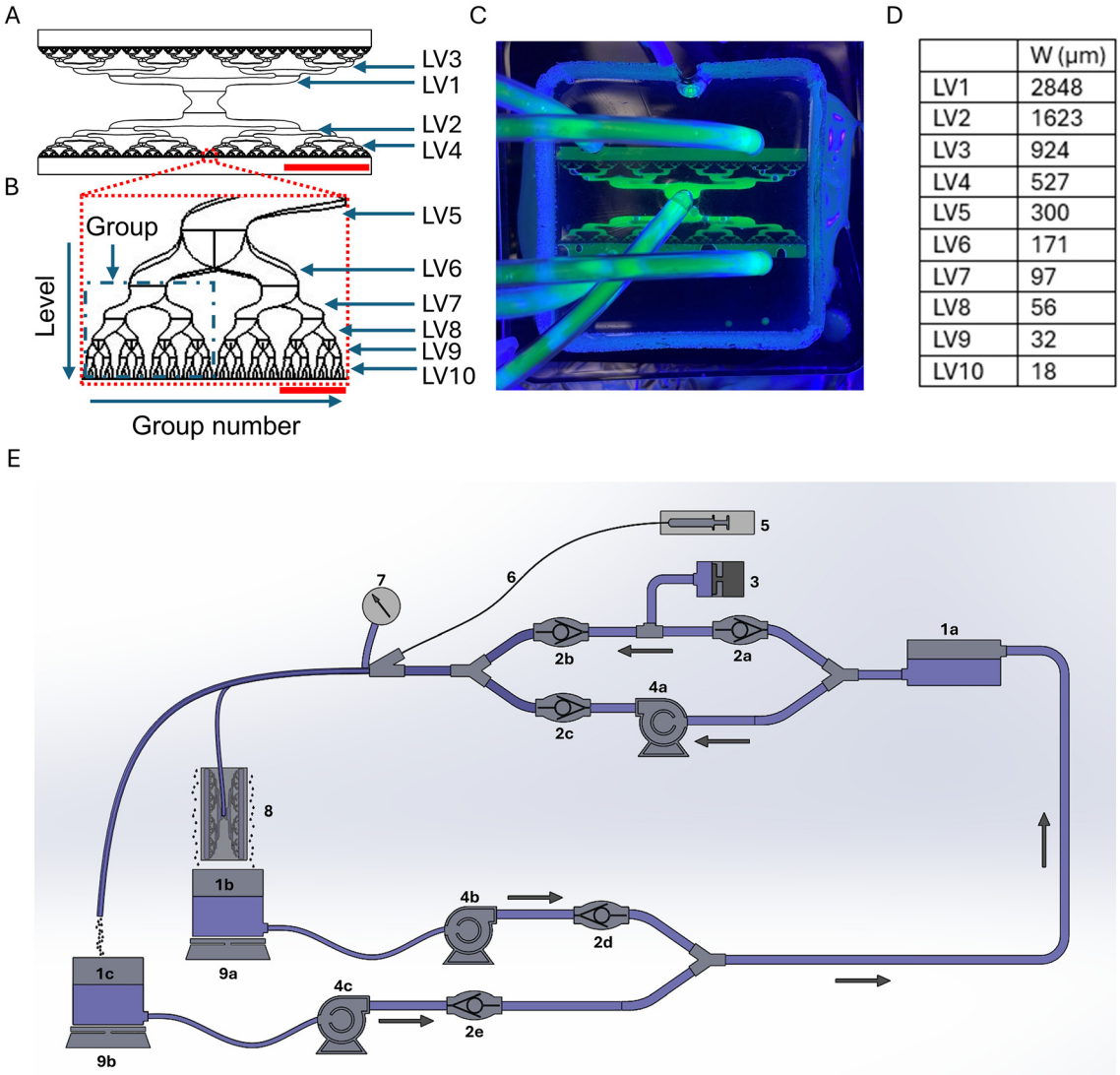

	W (μm)
LV1	2848
LV2	1623
LV3	924
LV4	527
LV5	300
LV6	171
LV7	97
LV8	56
LV9	32
LV10	18

Fig. 3 Phantom model design and perfusion system. (A) Schematic of the tumor mode (scale bar: 10 mm); (B) local detail and group information of the tumor model (scale bar: 300 μm); (C) photograph of the tumor model during static leak testing with fluorescent dye; (D) width of each level of branch; (E) Perfusion system schematic: 1a–c, reservoirs; 2a–e, 1-way valves; 3, pulsatile pump; 4a–c, centrifugal pumps; 5, syringe pump; 6, delivery catheter; 7, pressure transducer; 8, tumor model; 9a, 9b, laboratory scales.

pump was used for all administrations to achieve precise injection rates and dosages.

Following administration, the system was allowed to perfuse for several minutes to ensure that MS deposition was complete. Next, the microcatheter was removed, the flow rates were again allowed to reach steady-state, and the final post-embolization flow rates were recorded. Finally, a pinch valve was closed to stop flow to the tumor model, which was then disconnected from the hepatic vascular system and subsequently imaged using a microscope camera on an *x*–*y* stage. For each test, individual micrographs were stitched together using custom MATLAB scripts (MathWorks, Natick, MA, USA) to form a single mosaic image. Each test was run in triplicate.

To evaluate the results, branches of the model were categorized based on their sizes and the distance from the injection location. As shown in Fig. 3A and B, the branches closest to the inlet were named Level 1, then Level 2, Level 3, and so on. Therefore, the smallest and furthest branches were named Level 10. To better summarize the penetration depths of the embolization results, all the branches Level equal or larger than Level 6 were grouped together. The penetration depth of each group was determined by the level of branches inside the group with the most distal penetration of MSs. The width of each level is listed in Fig. 3D.

2.3 Statistical analysis

One-way analysis of variance (ANOVA) was performed in GraphPad Prism 10 (GraphPad Software, CA, USA) to assess statistical differences between groups. A *p*-value of less than 0.05 was considered significant. Data are presented as the

mean ± standard deviation (STD) or mean ± standard error of the mean (SEM), unless stated otherwise.

3. Results and discussion

3.1 Size and morphology

Ca-Alg MSs with varying concentrations of Ta (0%, 5%, 10%, 20%, and 30%) were engineered using a gas-shearing method[7] and observed using a microscope (Fig. 4A–E).

The diameter measurements show that the inclusion of Ta did not affect the size distribution of the MSs within each batch of synthesis. The diameters of 1Alg2Ca0Ta, 1Alg2Ca5Ta, 1Alg2Ca10Ta, 1Alg2Ca20Ta, and 1Alg2Ca30Ta (Fig. 4F) are 169.13 ± 10.16 μm, 204.90 ± 5.86 μm, 254.27 ± 6.94 μm, 211.04 ± 10.36 μm, and 261.82 ± 20.33 μm, respectively. The standard deviations (STD) of 1Alg2Ca5Ta, 1Alg2Ca10Ta, and 1Alg2Ca20Ta are all lower than 6% of the mean diameters, indicating uniformly distributed sizes. This size consistency is important for predictable embolization outcomes, as a narrow size range ensures selective targeting of blood vessels. Studies have shown that uniform size of MSs is critical to precise embolization as they prevent catheter blockage and ensure predictable distal penetration.[19] Compared to commercially available MSs, which typically exhibit broader size distributions (100–300 μm for DC Bead™), the Ta@Ca-Alg MSs demonstrate superior consistency within each synthesized batch. However, the MSs containing 30% Ta (1Alg2Ca30Ta) exhibit a larger STD (8% of the mean diameter), which suggests greater variability in MS sizes. This is likely due to the high concentration of Ta in the sodium alginate solution, which frequently obstructed the inner layer of the concentric needle during fabrication. The irregular flow may have resulted in inconsistent droplet formation, leading to increased size variability.

The variation in MS sizes observed among different Ta concentrations primarily results from slight changes in the air flow rate through the outer layer of the co-axial needle used during synthesis. Higher air flow rate produces higher shear force which leads to smaller MSs, whereas lower air flow rate generates larger MSs. During synthesis, higher Ta content rendered higher frequent occlusion of the co-axial needle, which requires additional fine tuning of the air flow rate. It is hypothesized that this fluctuation of air flow rate caused the variation of MS diameters. It is important to note that MSs with each Ta concentration represent a unique formulation, and that the

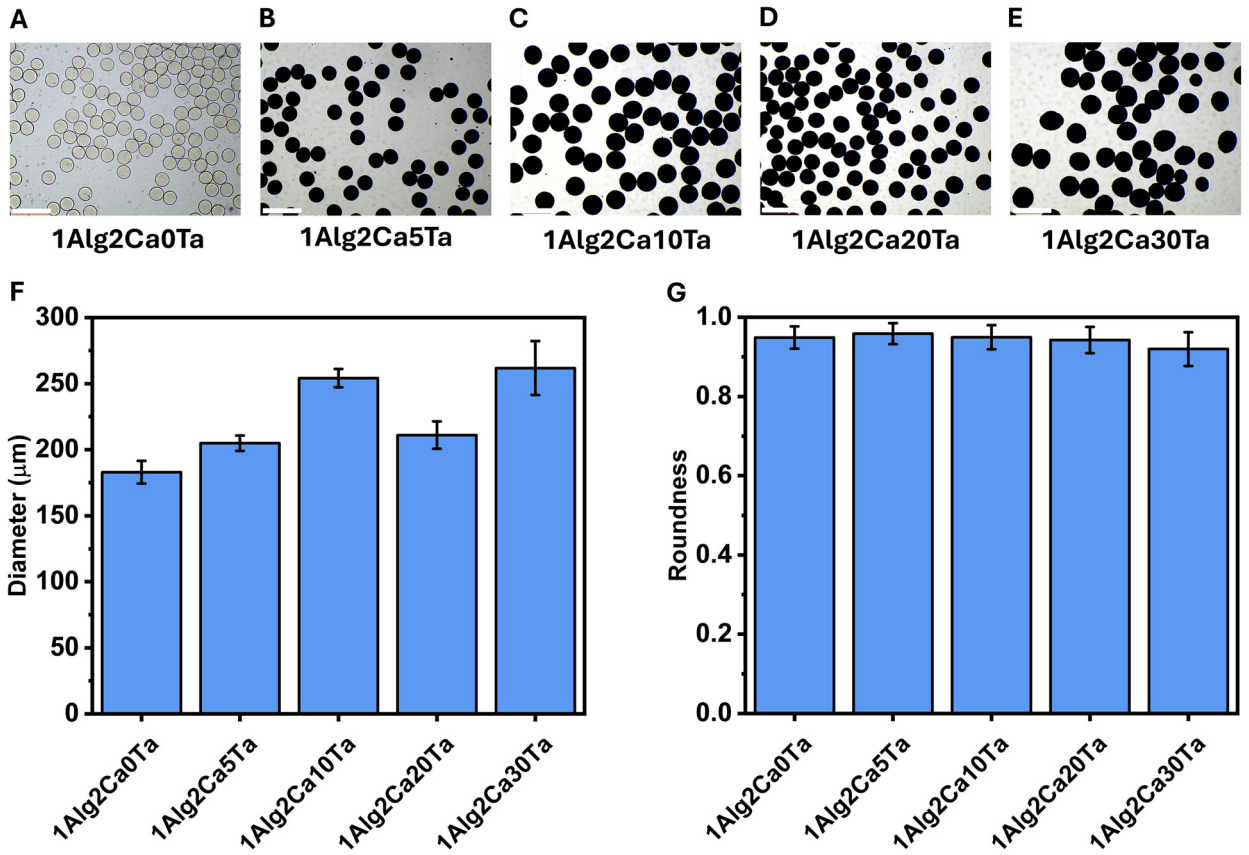

Fig. 4 Size and morphology of Ta@Ca-Alg MSs. (A–E) Representative images of 1Alg2Ca0Ta, 1Alg2Ca5Ta, 1Alg2Ca10Ta, 1Alg2Ca20Ta, 1Alg2Ca30Ta. Scale bars: 500 μm. (F and G) Diameters and roundness of MSs. Data are presented as mean ± standard deviation (STD) ($324 \leq n \leq 710$).

sizes of MSs with the same formulation are consistent. It is not expected that this limited variation will affect the embolization performance significantly.

The spherical shape of MSs plays a crucial role in the TAE process, as non-spherical MSs tend to interlock, obstruct the microcatheter, and pose challenges in being transported by blood flow to distant sites.[19] The roundness of 1Alg2Ca0Ta, 1Alg2Ca5Ta, 1Alg2Ca10Ta, 1Alg2Ca20Ta, 1Alg2Ca30Ta are 0.95 ± 0.03, 0.96 ± 0.03, 0.95 ± 0.03, 0.94 ± 0.03, 0.92 ± 0.04, respectively. Despite slightly elevated variability (a roundness STD at 4.6% of mean) observed with 1Alg2Ca30Ta, the roundness of all types of MSs (Fig. 4G) are close to 1, indicating that they all exhibit highly spherical shapes, which is essential for smooth navigation through blood vessels and preventing complications such as catheter blockage or premature embolization.[12,18] Due to the higher variability in size along with fabrication difficulties at high Ta loading (*e.g.*, needle clogging), 1Alg2Ca30Ta MSs were excluded from further studies. In contrast, 1Alg2Ca5Ta, 1Alg2Ca10Ta, and 1Alg2Ca20Ta demonstrated more consistent morphological characteristics, highlighting their potential for embolization.

3.2 Swelling

The swelling behavior of the MSs is crucial during the TAE process as it determines the size of blood vessels the MS can block, as well as the physical and mechanical properties of MS in blood vessels. As shown in Fig. 5A–E, all MSs swelled homogeneously, while the shape remained spherical. Swelling ratios (Fig. 5F) indicated that all the MSs swelled significantly in saline within the first 4 hours with the swelling ratio ranging between 1.47 ± 0.04 (1Alg2Ca10Ta) and 1.62 ± 0.05 (1Alg2Ca5Ta). After 8 hours their sizes were considered stable. This rapid initial swelling suggests that ion exchange between Na^+ ions from the saline and Ca^{2+} ions within the alginate matrix occurs predominantly within the early time points, leading to water uptake and expansion of the MSs. Importantly, despite swelling, the MSs maintained their spherical shape throughout the process, which is critical for smooth catheter delivery and precise embolization.

The swelling ratio of 1Alg2Ca0Ta, 1Alg2Ca5Ta, 1Alg2Ca10Ta, and 1Alg2Ca20Ta at 72 hours are 1.56 ± 0.05, 1.62 ± 0.04, 1.46 ± 0.03, and 1.51 ± 0.08, respectively. The crosslinking densities of all the MSs were considered similar due to consistent concentration of sodium alginate used during the synthesis. Hence, the swelling ratios of MSs were not significantly changed among the four types of MSs. However, since high concentration of Ta microparticles could occupy spaces within the polymer matrix, restricting the movement of polymer chains and limiting their ability to expand when exposed to water, the addition of Ta may decrease the swelling ratio. This could be observed by comparing

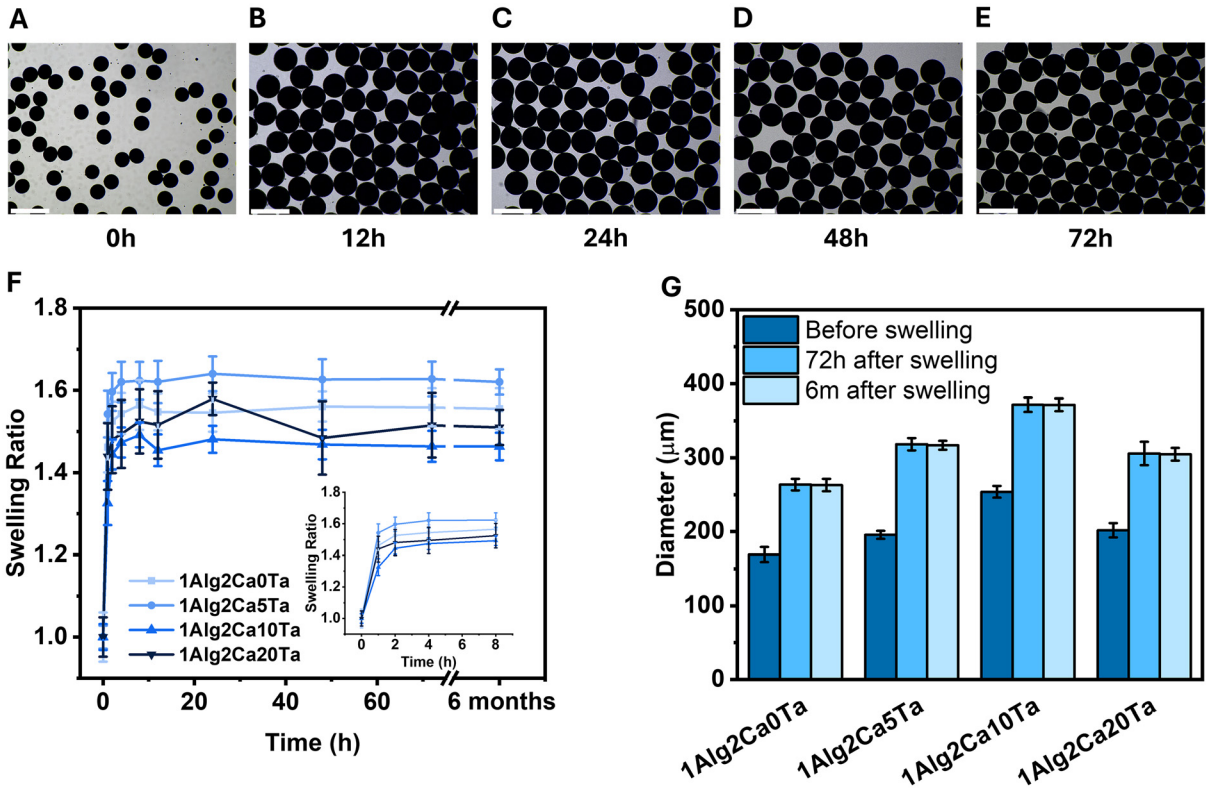

Fig. 5 (A–E) Representative microscopic images of 1Alg2Ca5Ta after 0 h, 12 h, 24 h, 48 h, and 72 h of swelling. Scale bar: 500 μm. (F) Swelling ratios of 1Alg2Ca0Ta, 1Alg2Ca5Ta, 1Alg2Ca10Ta, and 1Alg2Ca20Ta at 0 h, 1 h, 2 h, 4 h, 8 h, 12 h, 24 h, 48 h, 72 h, and 6 months. (G) Diameters of 1Alg2Ca1ICG, 1Alg2Ca5Ta, 1Alg2Ca10Ta, and 1Alg2Ca20Ta before and after swelling obtained from microscopic images. Data are presented as mean ± STD ($181 \leq n \leq 479$).

the swelling of 1Alg2Ca5Ta and 1Alg2Ca20Ta for which the original sizes (204.90 ± 5.86 μm and 211.04 ± 10.36 μm respectively) are similar, while 1Alg2Ca20Ta has a lower swelling ratio. Meanwhile, a lower concentration of Ta may not occupy enough space to restrict the movement of polymer chains. Instead, the Ta microparticles loosen the alginate network slightly, making it more permeable to sodium ions and increasing swelling. This can be shown on 1Alg2Ca5Ta which has the highest swelling ratio. While this increased swelling contributes to lower mechanical integrity, microscopic analysis of all types of MSs after six months (Fig. 5F and G) showed no measurable changes in diameter, suggesting potential long-term physical stability.

The sizes of MSs also have an impact on the swelling ratio. Smaller MSs such as 1Alg2Ca5Ta (204.90 ± 5.86 μm) and 1Alg2Ca20Ta (211.04 ± 10.36 μm) have larger specific surface areas (surface area to volume ratio) in comparison with 1Alg2Ca10Ta (254.27 ± 6.94 μm) so that the Ca^{2+} ions have more tendency to interact with Na^{+} ions which consequently have higher swelling ratios.[35]

3.3 Density

The density of MSs is a critical property as it is related to the dispersity in media and occlusion of the microvasculature. MSs with lower density remain suspended, leading to distal penetration,[26] while higher density MSs tend to settle quickly, potentially causing diminished handling.[19] Densities of 1Alg2Ca1ICG, 1Alg2Ca5Ta, 1Alg2Ca10Ta, and 1Alg2Ca20Ta before and after swelling were measured to assess the impact of Ta concentrations on the MS density (Fig. 6). The densities of 1Alg2Ca1ICG, 1Alg2Ca5Ta, 1Alg2Ca10Ta, and 1Alg2Ca20Ta before swelling are 1.03 ± 0.00 g cm^{-3}, 1.20 ± 0.02 g cm^{-3}, 1.35 ± 0.01 g cm^{-3}, and 1.59 ± 0.07 g cm^{-3}, respectively. The densities of the MSs generally increased with the increasing concentration of Ta. This trend is expected, as Ta is a high-density material (16.65 g cm^{-3})[36] that contributes to the overall mass of the MSs.

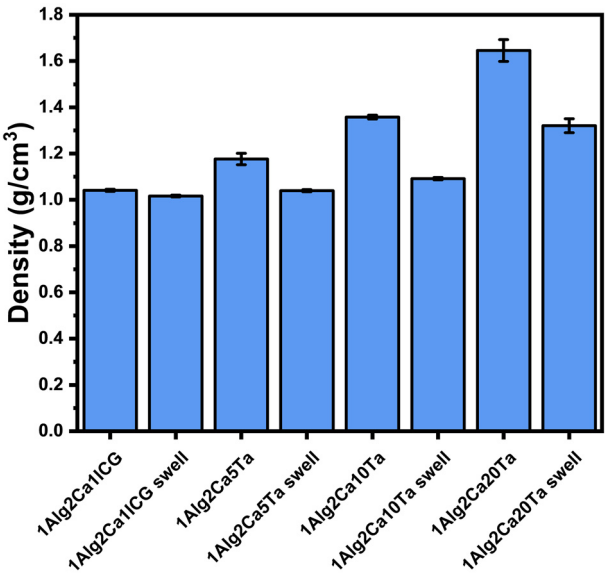

Fig. 6 Density of 1Alg2Ca1ICG, 1Alg2Ca5Ta, 1Alg2Ca10Ta, 1Alg2Ca20Ta before and after swelling. Data are presented as mean ± STD (n = 10).

After swelling, the densities of 1Alg2Ca1ICG, 1Alg2Ca5Ta, 1Alg2Ca10Ta, and 1Alg2Ca20Ta reduced to 1.01 ± 0.00 g cm^{-3}, 1.04 ± 0.00 g cm^{-3}, 1.09 ± 0.01 g cm^{-3}, and 1.32 ± 0.03 g cm^{-3}, respectively. This decrease is attributed to the increased water content within the MS matrix, diluting the effect of Ta on overall density. However, the trend of increasing density with Ta concentration remains consistent even after swelling, indicating that Ta amount continues to influence the final density of the swollen MSs.

The low standard deviations (all below 5% of the mean) confirm that the MSs within each formulation exhibit a uniform density, ensuring consistent suspension and sedimentation behavior. This is a crucial property for embolization procedures, as MSs with uniform densities will have predictable movement within blood flow, reducing the risk of premature settling or uneven embolization.[19,22]

The controllable density of MSs plays an important role, which directly affects their behavior during injection and delivery to the target site. With lower density,[37] the MSs may not readily settle in the desired location, potentially affecting the treatment efficacy. High-density MSs tend to settle quickly after suspension, which can cause clumping or blockage in the catheter, complicating the injection process.[19] Jernigan *et al.*[26] compared resin MSs (density = 1.57 g cm^{-3}) and glass MSs (density = 2.52 g cm^{-3}) by injecting them into a tumor model. Their results showed that, under the same embolization conditions, MSs with lower density have higher penetration depth. However, since the density of blood is 1.060 g cm^{-3}, MSs that are too low in density may float on the surface instead of settling down in the target blood vessel. The densities of 1Alg2Ca10Ta and 1Alg2Ca20Ta are both higher than the blood but lower compared to the resin MSs. This ensures that the MSs remain well-suspended during the procedure, allowing smooth and predictable catheter injections, and efficient MSs delivery to the intended vasculature without premature settling or being washed away.[38]

3.4 Imageability

The incorporation of Ta microparticles significantly enhances the radiopacity of the MSs, allowing them to be effectively imaged under X-ray. OMNIPAQUE 350 (iohexol) was used as the control because it is one of the clinically used contrast agents that is recommended by the commercially available embolic agents (LC Bead LUMI™, Boston scientific, Marlborough, Massachusetts). The iohexol concentration of 100% OMNIPAQUE 350 is 755 mg mL^{-1}, which is equivalent to 350 mg mL^{-1} of iodine and is the highest concentration of OMNIPAQUE used clinically. The equivalent iodine concentration of 50% of OMNIPAQUE 350 (diluted with deionized water) is 175 mg mL^{-1}, which is toward the lower end of a clinically used concentration. The pre-swelling radiopacity measurements, expressed in grayscale values, demonstrate that all Ta-loaded MSs exhibit excellent radiopacity comparable to 100% OMNIPAQUE 350 (gray scale: 228.78 ± 1.15).

Specifically, 1Alg2Ca5Ta, 1Alg2Ca10Ta, and 1Alg2Ca20Ta (Fig. 7) showed values of 210.72 ± 1.93, 223.12 ± 3.44, and 239.23 ± 1.69, respectively, confirming that even the lowest Ta concentration provides sufficient contrast for X-ray imaging. Notably, 1Alg2Ca20Ta exceeded the radiopacity of 100% OMNIPAQUE, suggesting its potential for superior visibility during embolization.

After swelling, a decrease in radiopacity was observed due to the dilution effect—swelling increases the volume of MSs, thereby reducing the Ta concentration per unit volume. The most significant reduction was seen in 1Alg2Ca5Ta (from 210.72 ± 1.93 to 165.71 ± 0.30), which decreased by 21.4%, potentially impacting its effectiveness for long-term imaging. 1Alg2Ca10Ta (204.40 ± 1.21) retained radiopacity comparable to 50% OMNIPAQUE (207.54 ± 0.14), while 1Alg2Ca20Ta (237.41 ± 0.28) exhibited minimal reduction (0.76% decrease) and remained even more radiopaque than 100% OMNIPAQUE.

These results indicate that increasing Ta content in MSs effectively mitigates radiopacity loss due to swelling. 1Alg2Ca20Ta emerges as the most stable formulation in terms of radiopacity retention, making it highly suitable for applications requiring prolonged imaging. However, balancing Ta concentration with other factors such as density, swelling behavior, and embolic performance is necessary and require further study to ensure optimal clinical efficacy.

3.5 *In vitro* studies

3.5.1 Hemocompatibility. The evaluation of hemocompatibility is crucial when assessing new embolic materials because of their direct interaction with blood. Hemolysis, the destruction of red blood cells, can result in hemolytic anemia.[39] The hemolysis test is considered a simple and reliable method for determining hemocompatibility, with a hemolysis rate below 5% being considered acceptable.[33] As shown in Fig. 8A, the hemolysis rates of all the MSs were lower than 0.5%, indicating excellent hemocompatibility. Statistical analysis showed that there was no significant change in hemolysis rate when the Ta concentration changes in MSs. The observed hemolysis rates are: 0.246% ± 0.039%, 0.367% ± 0.056%, 0.343%±0.055%, 0.116% ± 0.052% for 1Alg2Ca0Ta, 1Alg2Ca5Ta, 1Alg2Ca10Ta, and 1Alg2Ca20Ta, respectively. These values indicate that the addition of Ta does not significantly influence the hemolysis rate, as statistical analysis revealed no significant differences across the formulations, suggesting that all formulations are hemocompatible.

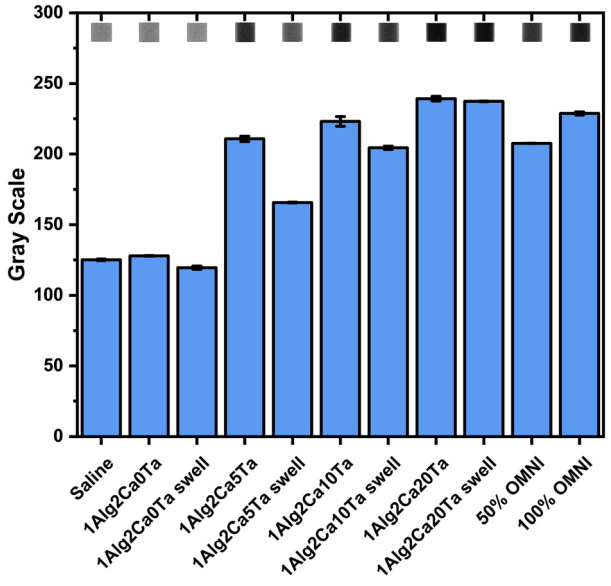

Fig. 7 Quantitative gray scale of X-ray images of 1Alg2Ca0Ta, 1Alg2Ca5Ta, 1Alg2Ca10Ta, 1Alg2Ca20Ta before and after swelling obtained from AMI-HTX. Saline, 50% OMNIPAQUE, and 100% OMNIPAQUE were used as controls. Data are presented as mean ± STD (n = 3).

3.5.2 Sterility. Sterility is paramount in the use of embolic agents due to the significant risk of infection associated with interventional procedures which can lead to serious outcomes, including liver abscesses and endometritis.[40] The OD600 nm absorption rates of all MSs shown in Fig. 8B are close to 0, which demonstrates that no bacterial growth was detected in any of the MS samples, confirming their inherent sterility.

3.5.3 Cell viability. Biocompatibility is a key consideration for embolic MSs as they come into direct contact with tissues and blood vessels during TAE. The WST-1 assay was conducted to assess the biocompatibility of the MSs by evaluating the viability of L929 fibroblast cells after exposure to MS extractions. All MS formulations (Fig. 8C) resulted cell viabilities above 70%, confirming their non-cytotoxic nature according to ISO 10993-5 standards.[32]

The WST-1 assay results strongly support the biocompatibility of all MS formulations, making them viable candidates for embolization procedures. The presence of Ta does not induce cytotoxicity even at its highest tested concentration. These findings further validate the hemocompatibility and sterility results, reinforcing the safety profile of these MSs for potential clinical use.

A live and dead assay was further conducted to visualize the viability of L929 cells after contact with 100% extracts of MSs overnight. The blue and green dots shown in Fig. 8D represent live and dead cells respectively. As shown in Fig. 8E, all MS formulations exhibited cell viabilities above 97%, which is comparable to the medium-alone control, indicating that none of the MSs induced significant cytotoxicity.

The minor variation in cell viability between different formulations is not statistically significant, further confirming that the inclusion of Ta did not negatively impact biocompatibility. These findings again support MSs suitability as safe embolic agents.

3.6 Mechanical properties

The mechanical properties of MSs are of great importance in their performance during TAE, influencing their ability to navigate blood vessels, withstand physiological forces, and effectively occlude targeted vessels. Fluidic force microscopy

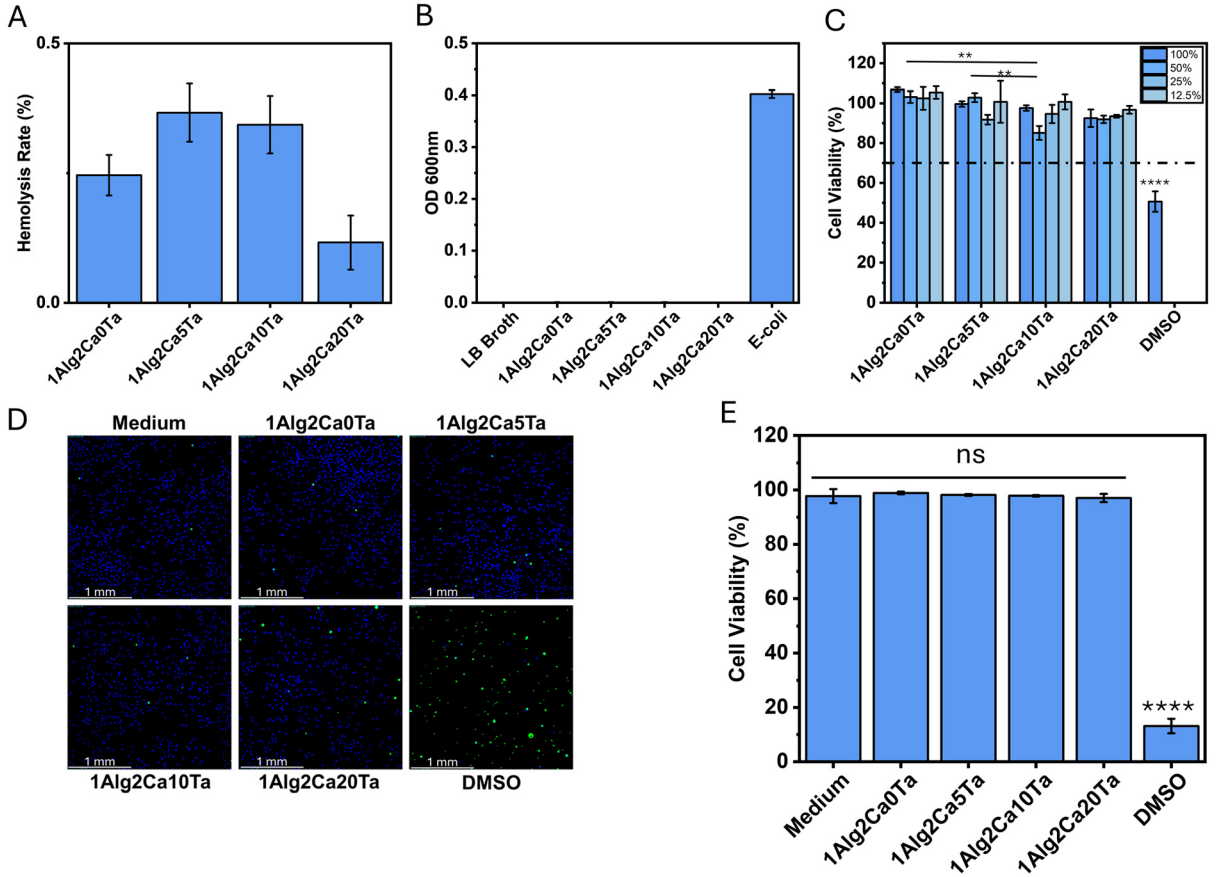

Fig. 8 Biological characterization of 1Alg2Ca0Ta, 1Alg2Ca5Ta, 1Alg2Ca10Ta, and 1Alg2Ca20Ta. (A) Hemolysis rate indicates good hemocompatibility of all the materials. (B) Sterility test shows no bacteria growth for all MSs, confirming inherent sterility. *E. coli* and LB broth were used as positive and negative controls (C) WST-1 assay with 100%, 50%, 25%, 12.5% extraction from all MSs. DMSO and medium alone were used as positive and negative controls. (D) Representative microscopic-fluorescence images obtained from cell live & dead assay (blue: live, green: dead). (E) Quantitative results of cell live & dead assay summarized from microscopic-fluorescence images. DMSO and medium alone were used as positive and negative controls. Data are presented as mean ± STD. (n = 4 for A and B, n = 3 for C, n = 6 for E). ns: not significant, $P > 0.05$; **$P \leq 0.01$; ****$P < 0.0001$.

(FluidFM) was employed to quantify the Young's modulus of the MSs.

The analysis of unloading curves (Fig. 9A) ensures that only elastic deformation is considered. It can be observed from the representative indentation results (Fig. 9B and C) that the Young's moduli obtained from the 25 points are within a reasonably consistent with 76% of which fell into the range between 4 kPa and 6 kPa. This demonstrates that the area of the 1Alg2Ca20Ta MS being indented was at the peak of the MS, which ensured the accuracy and precision of the results. The average Young's moduli of 1Alg2Ca0Ta, 1Alg2Ca5Ta, 1Alg2Ca10Ta, and 1Alg2Ca20Ta are 12.54 ± 3.06 kPa, 4.64 ± 0.54 kPa, 9.82 ± 1.51 kPa, and 6.47 ± 0.88 kPa, respectively (Fig. 9D). All the standard deviations are within 15% of the mean values except 1Alg2Ca0Ta, which is 24% of the mean value.

These results indicate that the addition of Ta influences the mechanical properties of the MSs, though not in a strictly linear manner. 1Alg2Ca5Ta exhibits the lowest Young's modulus, suggesting that a small amount of Ta may disrupt the internal crosslinking network of calcium alginate, making the MSs more deformable. Conversely, at higher Ta concentrations (10% and 20%), the Young's modulus increases, which may be attributed to the high Young's modulus of Ta (186 GPa).[36]

The higher standard deviation (24% of the mean) for 1Alg2Ca0Ta suggests greater variability in mechanical properties, potentially due to nonuniform surface change during the swelling. In contrast, all Ta@Ca-Alg MSs exhibited standard deviations within 15% of the mean, indicating more uniform mechanical behavior post swelling, presumably as a result of the addition of Ta microparticles that stabilized the alginate matrix.[41]

For practical use, a lower Young's modulus suggests greater deformability, which can be beneficial for smooth passage through microcatheters and capillaries. However, excessive softness may lead to undesired compression or fragmentation under physiological pressure. 1Alg2Ca5Ta, 1Alg2Ca10Ta, and 1Alg2Ca20Ta demonstrate Young's modulus close to that of capillary (3.0 kPa–10.0 kPa),[42] making them potentially suit-

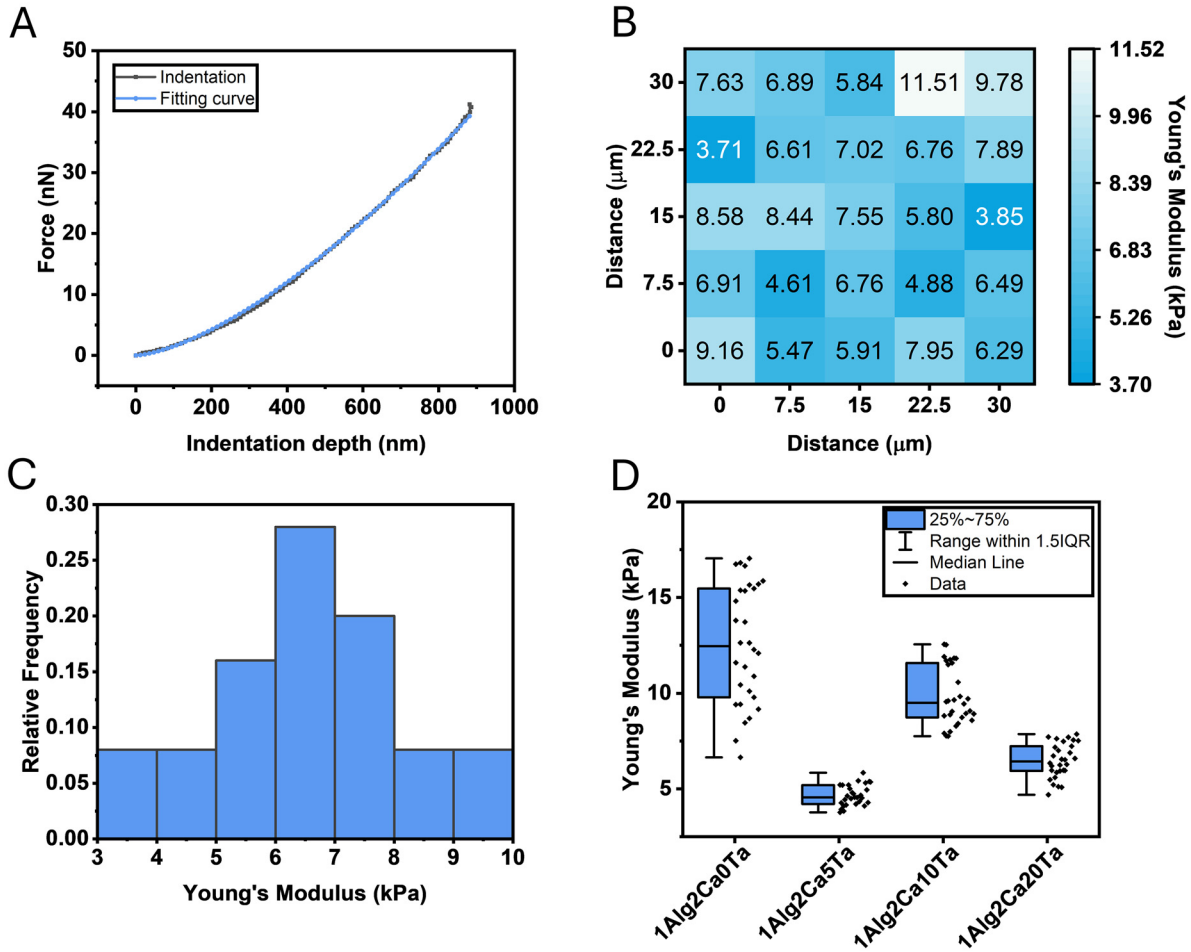

Fig. 9 Mechanical testing of MSs using FluidFM. (A) Representative force–indentation curve (unloading) and fitting curve of a single point on a 1Alg2Ca20Ta MS; (B) representative modulus distribution map for the 1Alg2Ca20Ta; (C) histogram of Young's modulus distribution for the same MS presented in B; and (D) summary of Young's modulus of all Ta@Ca-Alg MSs. Data are presented as mean ± STD (n = 28 for D).

able candidates for distal embolization (*i.e.*, tumor and vascular embolization), as they can navigate through tortuous vessels effectively while maintaining structural integrity for stable occlusion.

The Young's modulus of Ta@Ca-Alg MSs ranges between 4.64 ± 0.54 kPa and 12.54 ± 3.06 kPa, comparable to or even stiffer than some clinically utilized embolic agents, such as gelatin-based and polyvinyl alcohol (PVA) MSs, which exhibit moduli as low as ~1 kPa.[5,23] Microscopic evaluations after six months of immersion in saline showed no observable changes in MS diameter, suggesting potential long-term mechanical stability.

3.7 Microvasculature phantom testing

A preliminary phantom test was conducted to simulate the clinical embolization process within a physiologically relevant PDMS hepatic tumor model. The model replicates the multi-scale nature of the systemic circulation, from large arteries down to precapillary vessels, providing a controlled environment to study embolic behavior. The use of 1Alg2Ca10Ta and 1Alg2Ca20Ta was due to their higher Young's modulus and radiopacities compared with 1Alg2Ca5Ta.

Following administration, both MS types effectively occluded flow through the tumor model, as indicated by a post-injection outlet flow rate of 0 mL min^{-1} for three repetitive tests of 1Alg2Ca10Ta and 0.8, 2, and 3 mL min^{-1} for the tests of 1Alg2Ca20Ta, confirming excellent embolization. The measured diameters of 1Alg2Ca10Ta (371.6 ± 8.5 μm) and 1Alg2Ca20Ta (304.7 ± 8.6 μm) (Fig. 5G) suggest that these MSs should ideally lodge within channels between Level 4 (527 μm) and Level 5 (300 μm) of the phantom. However, due to aggregation and mechanical deformation during flow, MSs were observed to occlude vessels at a range of levels (Fig. 10A and 11A). Notably, deformation was consistently observed at the embolization front, likely contributing to the effective occlusion observed across all tests.

For 1Alg2Ca10Ta (Fig. 10D–F), both upper and lower branches of the model showed similar embolization patterns due to their mirrored geometry. Most branches were occluded at Level 5 (Fig. 10B) and Level 6 (Fig. 10C), with a smaller

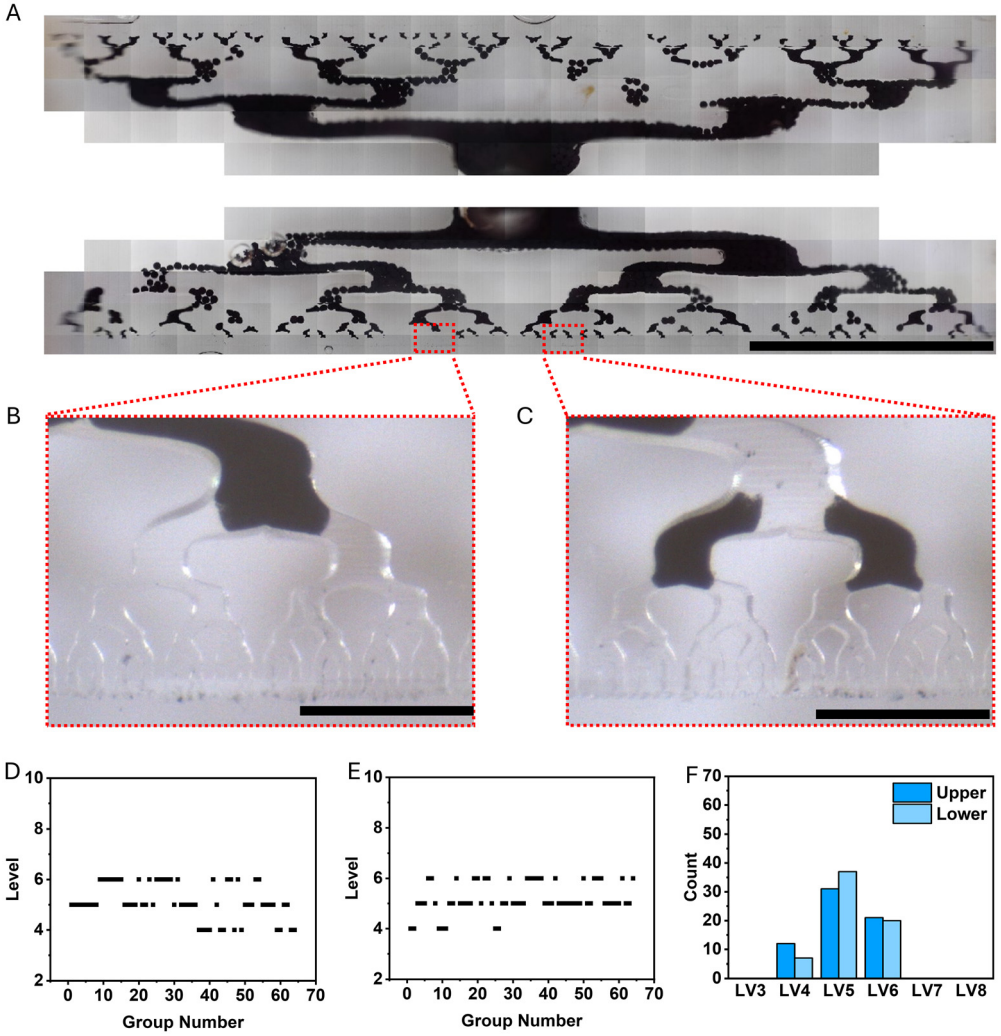

Fig. 10 Results of one of three repeated phantom test with 1Alg2Ca10Ta. (A) Representative microscopic image showing phantom model after injection of 1Alg2Ca10Ta. (Scale bar: 10 mm); (B) the branches were successfully embolized with 1Alg2Ca10Ta at level 5. (Scale bar: 500 μm); (C) the branches were successfully embolized with 1Alg2Ca10Ta at level 6; (D and E) penetration depths (represented as levels) of 1Alg2Ca10Ta correspond to group number for the upper and lower branches respectively; (F) number counts of penetration depths (represented as levels) for 1Alg2Ca10Ta.

portion being occluded at Level 3. Across three replicate experiments (Fig. 11E), 85.7% of occlusions occurred at Level 5 or 6, 13.8% at Level 4, and only 0.5% reached Level 7 or 8. In comparison, 1Alg2Ca20Ta exhibited more consistent embolization depth across replicates (Fig. 11B–D), with 94.5%, 76.6%, and 98.4% of occlusions occurring at Level 3 or 4 in individual tests, respectively (Fig. 11D, S3, and S4†). The summarized number count of levels for 1Alg2Ca20Ta (Fig. 11E) shows that 94% of occlusions were confined to Level 3 or 4, and only 6% reached Level 5 or 6. Despite having a larger average diameter, 1Alg2Ca10Ta showed deeper penetration than 1Alg2Ca20Ta, which can be attributed to its lower Young's modulus, allowing for greater deformability and enhanced distal embolization.

These phantom model results provide valuable insight into the embolization performance of the Ta@Ca-Alg MSs, particularly with respect to their deformation-driven penetration and occlusion profiles. Both 1Alg2Ca10Ta and 1Alg2Ca20Ta demonstrated the ability to deform and traverse smaller vascular channels, which is advantageous for achieving deep tumor embolization. The MSs shown in Fig. 10B and C also exhibited deformability yet stable occlusion with no breakage, indicating their resistance to flow. The higher mechanical stability of 1Alg2Ca20Ta may contribute to more predictable and controlled occlusion, while higher deformability of 1Alg2Ca10Ta may lead to deeper penetration.

The use of biomimetic phantom testing, as demonstrated here, offers a robust and reproducible method for preclinical evaluation under physiologically relevant flow and pressure conditions. Such platforms serve as an essential intermediate step between material development and *in vivo* validation, offering advantages in safety, cost-efficiency, and experimental control.

Overall, the integration of optimized mechanical properties, tunable density, and intrinsic radiopacity in these MSs represents a significant advancement over conventional embolic

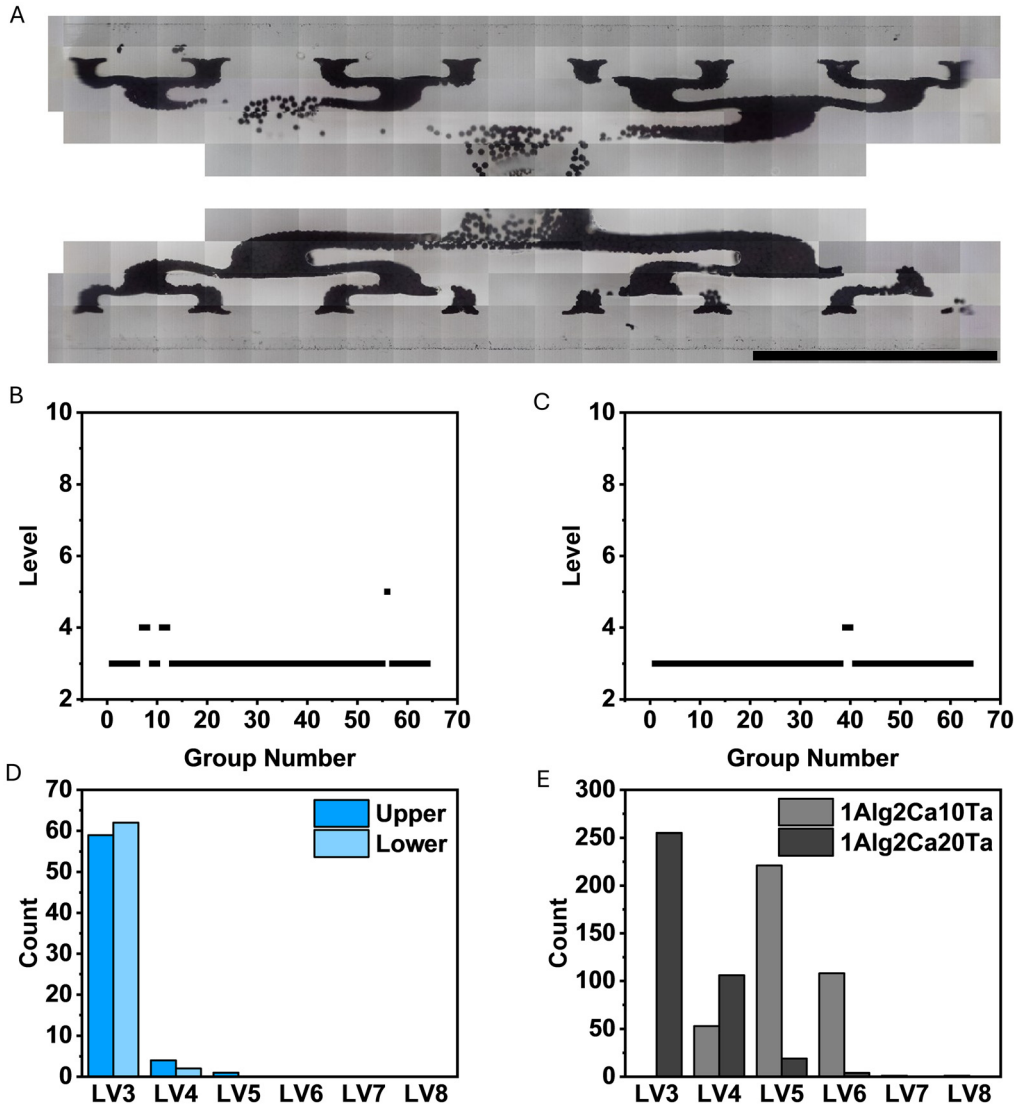

Fig. 11 Results of one of three repeated phantom tests with 1Alg2Ca20Ta and summarized level count. (A) Representative microscopic image showing phantom model after injection of 1Alg2Ca10Ta. (Scale bar: 10 mm); (B and C) penetration depths (represented as levels) of 1Alg2Ca20Ta correspond to group number for the upper and lower branches respectively; (D) number counts of penetration depths (represented as levels) for 1Alg2Ca20Ta; (E) summarized number counts of penetration depths for 1Alg2Ca10Ta and 1Alg2Ca20Ta with 3 repetitive tests.

agents. These features may enable more accurate vessel targeting, enhanced imaging guidance, and reduced off-target effects, thereby improving the safety and efficacy of embolization procedures. Future studies will include long-term mechanical stability testing and *in vivo* VX2 rabbit liver tumor models to assess embolic persistence and address concerns related to potential recanalization under sustained physiological pressures.

4. Conclusion

In this study, we successfully developed and characterized Ta@Ca-Alg MSs for TAE applications. The results demonstrated that the addition of Ta increased the density of the MSs as well as radiopacity, with 1Alg2Ca10Ta and 1Alg2Ca20Ta exhibiting radiopacity comparable to that of clinically used OMNIPAQUE contrast agents even after swelling. Mechanical characterization using FluidFM showed that Ta inclusion influenced the elasticity of the MSs, with 1Alg2Ca10Ta and 1Alg2Ca20Ta maintaining an optimal balance between deformability for catheter navigation and elasticity for stable occlusion. Phantom model testing further validated their embolization performance, demonstrating effective vessel occlusion. The results suggest that 1Alg2Ca10Ta and 1Alg2Ca20Ta are promising candidates for TAE, with 1Alg2Ca20Ta offering superior radiopacity and mechanical stability for long term embolization, while 1Alg2Ca10Ta offering higher deformability for better penetration depth.

Overall, this study provides insights into the development of radiopaque embolic MSs with tailored mechanical and imaging properties. This study represents one of the earliest comprehensive investigations into how Ta incorporation influences the mechanical properties of embolic microspheres, potentially setting a new benchmark for performance optimization in embolic agent design. These findings contribute to the advancement of embolization technologies, offering a novel biomaterial solution for improved image-guided TAE procedures with more control over the embolic agent behavior and ultimately, the treatment outcome.

Author contributions

Peng Chen: writing – original draft, validation, investigation, formal analysis, conceptualization. Shaphan Jernigan: writing – original draft, validation, investigation, formal analysis. Keren Zhao: writing – review & editing, validation, investigation, formal analysis. George Varghese P J: writing – review & editing, validation, investigation, formal analysis. Mitesha Saha: writing – review & editing, validation, investigation, formal analysis. Charles Kim: writing – review & editing. Amirhossein Arzani: writing – review & editing. Gregory Buckner: writing – review & editing. Jingjie Hu: writing – review & editing, supervision, project administration, funding acquisition, conceptualization.

Conflicts of interest

The authors declare that they have no known competing financial interests or personal relationships that could have appeared to influence the work reported in this paper.

Data availability

The data supporting this article have been included as part of the ESI.†

Acknowledgements

The authors are grateful to North Carolina State University, Haythornthwaite Foundation Research Initiation Grant, Kenan Institute (NCSU), the Ralph E. Powe Junior Faculty Enhancement Award, North Carolina Biotechnology Center, and the National Institutes of Health (NIBIB 1R03EB033633-01A1 and NIA 1R21AG083692-01) for financial support.

References

1 S. Lee, A. Ghosh, N. Xiao, A. C. Gordon, N. Heidarpour, B. Funaki and R. J. Lewandowski, Embolic Agents: Particles, *Semin. Intervent. Radiol.*, 2023, **40**, 315–322, DOI: **10.1055/s-0043-1769744**.

2 H. Choi, B. Choi, B. Yu, W. Li, M. M. Matsumoto, K. R. Harris, R. J. Lewandowski, A. C. Larson, S. K. Mouli and D.-H. Kim, On-demand degradable embolic microspheres for immediate restoration of blood flow during image-guided embolization procedures, *Biomaterials*, 2021, **265**, 120408, DOI: **10.1016/j.biomaterials.2020.120408**.

3 D. Ji, J. M. Park, M. S. Oh, T. L. Nguyen, H. Shin, J. S. Kim, D. Kim, H. S. Park and J. Kim, Superstrong, superstiff, and conductive alginate hydrogels, *Nat. Commun.*, 2022, **13**, 3019, DOI: **10.1038/s41467-022-30691-z**.

4 C. R. Brennecka, M. C. Preul, W. D. Bichard and B. L. Vernon, In Vivo Experimental Aneurysm Embolization in a Swine Model with a Liquid-to-Solid Gelling Polymer System: Initial Biocompatibility and Delivery Strategy Analysis, *World Neurosurg.*, 2012, **78**, 469–480, DOI: **10.1016/j.wneu.2011.10.029**.

5 T. A. Becker, D. R. Kipke and T. Brandon, Calcium alginate gel: A biocompatible and mechanically stable polymer for endovascular embolization, *J. Biomed. Mater. Res.*, 2001, **54**, 76–86, DOI: **10.1002/1097-4636(200101)54:1<76::AID-JBM9>3.0.CO;2-V**.

6 S. K. Bajpai and S. Sharma, Investigation of swelling/degradation behaviour of alginate beads crosslinked with Ca2+ and Ba2+ ions, *React. Funct. Polym.*, 2004, **59**, 129–140, DOI: **10.1016/j.reactfunctpolym.2004.01.002**.

7 P. Chen, G. Varghese, P. J. K. Zhao and J. Hu, Mechanical investigation of a Tandem embolization-visualization system for minimally invasive procedures, *J. Mech. Behav. Biomed. Mater.*, 2024, **160**, 106739, DOI: **10.1016/j.jmbbm.2024.106739**.

8 N. Farshidfar, S. Iravani and R. S. Varma, Alginate-Based Biomaterials in Tissue Engineering and Regenerative Medicine, *Mar. Drugs*, 2023, **21**, 189, DOI: **10.3390/md21030189**.

9 T. Han, L. Chen, F. Gao, S. Wang, J. Li, G. Fan, H. Cong, B. Yu and Y. Shen, Preparation of thrombin-loaded calcium alginate microspheres with dual-mode imaging and study on their embolic properties in vivo, *Eur. J. Pharm. Biopharm.*, 2023, **189**, 98–108, DOI: **10.1016/j.ejpb.2023.06.008**.

10 J. Zeng, L. Li, H. Zhang, J. Li, L. Liu, G. Zhou, Q. Du, C. Zheng and X. Yang, Radiopaque and uniform alginate microspheres loaded with tantalum nanoparticles for real-time imaging during transcatheter arterial embolization, *Theranostics*, 2018, **8**, 4591–4600, DOI: **10.7150/thno.27379**.

11 Q. Du, L. Li, Y. Liu, J. Zeng, J. Li, C. Zheng, G. Zhou and X. Yang, Fabrication of inherently radiopaque $BaSO_4$@BaAlg microspheres by a one-step electrospraying method for embolization, *J. Mater. Chem. B*, 2018, **6**, 3522–3530, DOI: **10.1039/C8TB00542G**.

12 K. V. Sharma, M. R. Dreher, Y. Tang, W. Pritchard, O. A. Chiesa, J. Karanian, J. Peregoy, B. Orandi, D. Woods, D. Donahue, J. Esparza, G. Jones, S. L. Willis, A. L. Lewis and B. J. Wood, Development of "Imageable", Beads for

Transcatheter Embolotherapy, *J. Vasc. Interv. Radiol.*, 2010, **21**, 865–876, DOI: 10.1016/j.jvir.2010.02.031.

13 M. Bendszus, R. Klein, R. Burger, M. Warmuth-Metz, E. Hofmann and L. Solymosi, Efficacy of trisacryl gelatin microspheres versus polyvinyl alcohol particles in the preoperative embolization of meningiomas, *American Journal of Neuroradiology*, 2000, **21**(2), 255–261.

14 X. Zhu, M. Duan, L. Zhang, J. Zhao, S. Yang, R. Shen, S. Chen, L. Fan and J. Liu, Liquid Metal–Enabled Microspheres with High Drug Loading and Multimodal Imaging for Artery Embolization, *Adv. Funct. Mater.*, 2023, **33**(18), 2209413, DOI: 10.1002/adfm.202209413.

15 J. Zeng, L. Li, H. Zhang, J. Li, L. Liu, G. Zhou, Q. Du, C. Zheng and X. Yang, Radiopaque and uniform alginate microspheres loaded with tantalum nanoparticles for real-time imaging during transcatheter arterial embolization, *Theranostics*, 2018, **8**, 4591–4600, DOI: 10.7150/thno.27379.

16 B. C. Thanoo, M. C. Sunny and A. Jayakrisnnan, Tantalum-loaded polyurethane microspheres for particulate embolization: preparation and properties, *Biomaterials*, 1991, **12**, 525–528, DOI: 10.1016/0142-9612(91)90154-3.

17 P. J. G. Varghese, P. Chen, K. Zhao, M. Saha and J. Hu, An Investigation on the Effect of Contrast Agents in the Chitosan-Nanoclay Shear Thinning Hydrogel for Trans-Catheter Arterial Embolization, *JOM*, 2024, **76**, 5643–5653, DOI: 10.1007/s11837-024-06729-6.

18 A. Laurent, M. Wassef, J.-P. Saint Maurice, J. Namur, J.-P. Pelage, A. Seron, R. Chapot and J.-J. Merland, Arterial Distribution of Calibrated Tris-Acryl Gelatin and Polyvinyl Alcohol Microspheres in a Sheep Kidney Model, *Invest. Radiol.*, 2006, **41**, 8–14, DOI: 10.1097/01.rli.0000188027.34400.f3.

19 M. Caine, D. Carugo, X. Zhang, M. Hill, M. R. Dreher and A. L. Lewis, Review of the Development of Methods for Characterization of Microspheres for Use in Embolotherapy: Translating Bench to Cathlab, *Adv. Healthcare Mater.*, 2017, **6**(9), 1601291, DOI: 10.1002/adhm.201601291.

20 R. Duran, K. Sharma, M. R. Dreher, K. Ashrafi, S. Mirpour, M. Lin, R. E. Schernthaner, T. R. Schlachter, V. Tacher, A. L. Lewis, S. Willis, M. den Hartog, A. Radaelli, A. H. Negussie, B. J. Wood and J.-F. H. Geschwind, A Novel Inherently Radiopaque Bead for Transarterial Embolization to Treat Liver Cancer - A Pre-clinical Study, *Theranostics*, 2016, **6**, 28–39, DOI: 10.7150/thno.13137.

21 Y. Tatari, T. A. Smith, J. Hu and A. Arzani, Optimizing distal and proximal splenic artery embolization with patient-specific computational fluid dynamics, *J. Biomech.*, 2024, **176**, 112320, DOI: 10.1016/j.jbiomech.2024.112320.

22 J. Hu, H. Albadawi, B. W. Chong, A. R. Deipolyi, R. A. Sheth, A. Khademhosseini and R. Oklu, Advances in Biomaterials and Technologies for Vascular Embolization, *Adv. Mater.*, 2019, **31**, 1901071, DOI: 10.1002/adma.201901071.

23 C. Y. Wang, J. Hu, R. A. Sheth and R. Oklu, Emerging Embolic Agents in Endovascular Embolization: An Overview, *Prog. Biomed. Eng.*, 2020, **2**, 012003, DOI: 10.1088/2516-1091/ab6c7d.

24 M. Y. Amarouch, J. E. Hilaly and D. Mazouzi, AFM and FluidFM Technologies: Recent Applications in Molecular and Cellular Biology, *Scanning*, 2018, **2018**, 1–10, DOI: 10.1155/2018/7801274.

25 A. Keister, A. Carfora, M. S. Patel, A. S. Zakeri, L. Mannix, D. G. Wheeler, P. S. Herson and S. M. Nimjee, Review: Preclinical Models of Large–Vessel Occlusion Stroke, *Stroke: Vasc. Interv. Neurol.*, 2024, **4**, 000604, DOI: 10.1161/SVIN.123.000604.

26 S. R. Jernigan, J. A. Osborne, C. J. Mirek and G. Buckner, Selective Internal Radiation Therapy: Quantifying Distal Penetration and Distribution of Resin and Glass Microspheres in a Surrogate Arterial Model, *J. Vasc. Interv. Radiol.*, 2015, **26**, 897–904, DOI: 10.1016/j.jvir.2015.02.022.

27 S. R. Miller, S. R. Jernigan, R. J. Abraham and G. D. Buckner, Comparison of Bolus Versus Dual-Syringe Administration Systems on Glass Yttrium-90 Microsphere Deposition in an In Vitro Microvascular Hepatic Tumor Model, *J. Vasc. Interv. Radiol.*, 2023, **34**, 11–20, DOI: 10.1016/j.jvir.2022.07.032.

28 S. R. Miller, S. R. Jernigan, R. J. Abraham and G. D. Buckner, Comparing Deposition Characteristics of Various Embolic Particles Using an In Vitro Prostate Microvasculature Model, *J. Vasc. Interv. Radiol.*, 2024, **35**, 1534–1543, DOI: 10.1016/j.jvir.2024.06.028.

29 J. Schindelin, I. Arganda-Carreras, E. Frise, V. Kaynig, M. Longair, T. Pietzsch, S. Preibisch, C. Rueden, S. Saalfeld, B. Schmid, J.-Y. Tinevez, D. J. White, V. Hartenstein, K. Eliceiri, P. Tomancak and A. Cardona, Fiji: an open-source platform for biological-image analysis, *Nat. Methods*, 2012, **9**, 676–682, DOI: 10.1038/nmeth.2019.

30 S. Moran, Fluid mechanics, in *An Applied Guide to Water and Effluent Treatment Plant Design*, Elsevier, 2018, pp. 53–58. DOI: 10.1016/B978-0-12-811309-7.00005-9.

31 P. Hermanowicz, M. Sarna, K. Burda and H. Gabryś, AtomicJ: An open source software for analysis of force curves, *Rev. Sci. Instrum.*, 2014, **85**, 063703, DOI: 10.1063/1.4881683.

32 International Organization for Standardization, Biological evaluation of medical devices—Part 5: Tests for in vitro cytotoxicity, ISO 10993-5: 2009, 2009.

33 International Organization for Standardization, Biological evaluation of medical devices—Part 4: Selection of tests for interactions with blood, ISO 10993-4: 2017, 2017.

34 G. D. Lowe, F. G. Fowkes, J. Dawes, P. T. Donnan, S. E. Lennie and E. Housley, Blood viscosity, fibrinogen, and activation of coagulation and leukocytes in peripheral arterial disease and the normal population in the Edinburgh Artery Study, *Circulation*, 1993, **87**, 1915–1920, DOI: 10.1161/01.CIR.87.6.1915.

35 D. Sadeghi, A. Solouk, A. Samadikuchaksaraei and A. M. Seifalian, Preparation of internally-crosslinked alginate microspheres: Optimization of process parameters and study of pH-responsive behaviors, *Carbohydr. Polym.*, 2021, **255**, 117336, DOI: 10.1016/j.carbpol.2020.117336.

36 Q. Wei, Z. L. Pan, X. L. Wu, B. E. Schuster, L. J. Kecskes and R. Z. Valiev, Microstructure and mechanical properties at different length scales and strain rates of nanocrystalline tantalum produced by high-pressure torsion, *Acta Mater.*, 2011, **59**, 2423–2436, DOI: **10.1016/J.ACTAMAT.2010.12.042**.

37 A. W. P. Maxwell, H. G. Mendoza, M. J. Sellitti, J. C. Camacho, A. R. Deipolyi, E. Ziv, C. T. Sofocleous, H. Yarmohammadi, M. Maybody, J. L. Humm, J. Schwartz, K. Juluru, M. P. Dunphy and F. E. Boas, Optimizing 90Y Particle Density Improves Outcomes After Radioembolization., *Cardiovasc. Intervent. Radiol.*, 2022, **45**, 958–969, DOI: **10.1007/s00270-022-03139-6**.

38 N. A. Nuzulia, T. Mart, I. Ahmed and Y. W. Sari, The Use of Microspheres for Cancer Embolization Therapy: Recent Advancements and Prospective, *ACS Biomater. Sci. Eng.*, 2024, **10**, 637–656, DOI: **10.1021/acsbiomaterials.3c00659**.

39 J. Phillips and A. C. Henderson, Hemolytic Anemia: Evaluation and Differential Diagnosis, *Am. Fam. Physician*, 2018, **98**, 354–361.

40 S. Y. Huang, A. Philip, M. D. Richter, S. Gupta, M. L. Lessne and C. Y. Kim, Prevention and management of infectious complications of percutaneous interventions, *Semin. Intervent. Radiol.*, 2015, **32**, 78–88, DOI: **10.1055/s-0035-1549372**.

41 K. Zdiri, A. Cayla, A. Elamri, A. Erard and F. Salaun, Alginate-Based Bio-Composites and Their Potential Applications, *J. Funct. Biomater.*, 2022, **13**, 117, DOI: **10.3390/jfb13030117**.

42 P. F. Salipante, S. D. Hudson and S. Alimperti, Blood vessel-on-a-chip examines the biomechanics of microvasculature, *Soft Matter*, 2022, **18**, 117–125, DOI: **10.1039/D1SM01312B**.

